

Mechanical modeling of pre-eruptive magma propagation scenarios at calderas

Lorenzo Mantiloni¹, Eleonora Rivalta², and Timothy Davis³

¹Helmholtz-Zentrum Potsdam - Deutsches Geoforschungszentrum

²GFZ

³University of Oxford

December 7, 2022

Abstract

Simulating magma propagation pathways requires both a well-calibrated model for the stress state of the volcano and models for dike advance within such a stress field. With the purpose of establishing a framework for calculating computationally efficient and flexible shallow magma propagation scenarios, we develop three-dimensional models for the stress state of volcanoes with complex topographies and edifice histories as well as a new simplified three-dimensional model of dike propagation using the stress state of the volcano as input. Next, we combine all these models to calculate shallow dike propagation scenarios for complex caldera settings. The resulting synthetic magma pathways and eruptive vent locations broadly reproduce the variability observed in natural calderas.

Mechanical modeling of pre-eruptive magma propagation scenarios at calderas

L. Mantiloni^{1,2}, E. Rivalta^{1,3}, T. Davis⁴

¹GFZ German Research Centre for Geosciences, Section 2.1 ‘Physics of Earthquakes and Volcanoes’,

Telegrafenberg, 14473 Potsdam, Germany.

²University of Potsdam, Potsdam, Germany

³Department of Physics and Astronomy, Alma Mater Studiorum University of Bologna, V.le Berti Pichat

8, 40126 Bologna, Italy

⁴University of Oxford, Oxford, United Kingdom

Key Points:

- We present numerical models of crustal stress state at calderas
- We develop a fast dike propagation model and validate it on a previous numerical model
- We combine our stress and dike models to simulate magma pathways at synthetic calderas

Corresponding author: Lorenzo Mantiloni, lorenzo@gfz-potsdam.de

Abstract

Simulating magma propagation pathways requires both a well-calibrated model for the stress state of the volcano and models for dike advance within such a stress field. With the purpose of establishing a framework for calculating computationally efficient and flexible shallow magma propagation scenarios, we develop three-dimensional models for the stress state of volcanoes with complex topographies and edifice histories as well as a new simplified three-dimensional model of dike propagation using the stress state of the volcano as input. Next, we combine all these models to calculate shallow dike propagation scenarios for complex caldera settings. The resulting synthetic magma pathways and eruptive vent locations broadly reproduce the variability observed in natural calderas.

Plain Language Summary

Understanding the pathways that bring magma from an underground chamber to the surface helps us preparing for future eruptions in volcanic areas. Dikes are fractures filled with magma and represent the most common mechanism of magma transport in the Earth's crust. Their trajectories may be curved if the Earth's crust is deformed by the load of topography or by tectonic forces. Here we first discuss a model of such deformation processes in volcanic regions with complex but mild topography. Then, we develop a simplified dike propagation model that we validate with a more sophisticated one. Next, we combine our models and simulate magma pathways in artificially-generated scenarios.

1 Introduction

Geophysical observations of ground deformation and seismicity in volcanic areas have highlighted how some eruptions are preceded by a long phase of magma propagation in the form of magma-filled dikes (Einarsson et al., 1980; Ebinger et al., 2010; Nakada et al., 2005; Uhira et al., 2005; Wright et al., 2012; Sigmundsson et al., 2015; Patrick et al., 2020; Cesca et al., 2020; Davis et al., 2021; Smittarello et al., 2022). Some recent dikes have propagated for over 70 km, reaching locations that had not experienced any fissure opening in decades or centuries; in some cases the ensuing lava flows have resulted in massive property damage (Patrick et al., 2020; Martí et al., 2022) or, in the extreme case of the 2021 eruption at Niyragongo, in hundreds of victims (Smittarello et al., 2022). The associated dike trajectories have also displayed a variety of geometries and spatial orientations, from horizontal to oblique to vertical, and shapes, from planar to segmented, curved or twisted (Branca et al., 2003; Bagnardi et al., 2013; Xu & Jónsson, 2014; Sigmundsson et al., 2015; Patrick et al., 2020; Davis et al., 2021; Dumont et al., 2022; Smittarello et al., 2022; Martí et al., 2022). In spite of the importance of this process, there are still no models to forecast, in three dimensions, the trajectory taken by magma during propagation in the shallow crust.

Our physical understanding and our models of dike trajectories have progressed significantly in the last decades. Both early (Anderson, 1937) and more recent works (Dahm, 2000a) have established that dike pathways are largely determined by the balance between the elastic stresses in the host rock and the buoyancy force resulting from the density contrast between magma and rock. As a rule of thumb, dikes open against the direction of the least-compressive principal stress axis (Ziv et al., 2000; Gudmundsson, 2002; Pollard et al., 2005); together with the external stresses, the buoyancy force determines the direction of propagation along the dike tip line (Weertman, 1971; Pollard, 1987; Rubin, 1995; Taisne et al., 2011; Rivalta et al., 2015; Townsend et al., 2017). The simplest 2D trajectories are streamlines perpendicular to the least-compressive stress axis (Anderson, 1937; Pollard, 1987), while the most sophisticated approaches model dikes as cracks steered in the direction of maximum strain energy release rate (Dahm, 2000a; Maccaferri et al., 2010, 2011). Dike trajectory models have recently evolved from two dimensional (2D)

(Anderson, 1937; O. H. Muller & Pollard, 1977; Pollard, 1987; Dahm, 2000a) to partially (Sigmundsson et al., 2015; Heimissson et al., 2015; Pansino et al., 2022), and, finally, fully three-dimensional (3D) by (Davis et al., 2020, 2021). The latter model extends to 3D the maximum strain energy release rate trajectory calculation approach introduced by Dahm (2000a); a 3D equivalent of the simple 2D streamline approaches is still missing.

The 3D model by Davis et al. (2020, 2021) has been applied to explain the counterintuitive trajectory of the 2018 dike at Sierra Negra, Galápagos. Importantly, Davis et al. (2021) confirmed the pivotal importance of a well-calibrated stress field in modelling dike trajectories: contributions from different stress-generating mechanisms, such as topographic gravitational loading and regional stress field, needed to be carefully adjusted in order to steer the dike on the observed trajectory. If we want to simulate 3D dike propagation at arbitrary volcanoes, we also need to determine their state of stress.

This problem was addressed by Rivalta et al. (2019), who suggested a stress inversion strategy which involves, first, establishing the relevant sources of stress for the specific volcano, and then, tuning their relative intensity so that simulated dikes starting from the known location of magma storage reach the known locations of past eruptive vents. This strategy was tested on Campi Flegrei caldera in Italy, using only 2D (plane strain) stress models and 2D streamlines for dike propagation.

Extending the stress calibration strategy by Rivalta et al. (2019) to 3D would pave the way to forecast dike pathways in 3D at any arbitrary volcano. A preliminary step is to set up 3D stress and dike trajectory models that are computationally efficient for the large number of simulations needed by the stress calibration procedure. In this study, we first develop computationally efficient 3D stress field calculations for scenarios with topographic reliefs. Then, we develop a fast, semi-analytical 3D dike propagation model that approximates the sophisticated model by Davis et al. (2020, 2021) but retains the simplicity of 2D streamlines and can also backtrack a dike trajectory from eruptive vent to magma chamber. Finally, we show how to integrate all these models to produce realistic pre-eruptive magma propagation scenarios. We focus on calderas, setting up synthetic topographies inspired by natural systems.

2 Method formulation

We now separately introduce our 3D stress and dike propagation models, and then describe how to combine them in dike propagation scenarios. We use the scenarios to calibrate some needed parameters and validate our propagation method. Finally, we run the propagation model for a set of increasingly complex settings. We assume a homogeneous, isotropic and linearly elastic medium as the host rock, described by rock density ρ_r , Young's modulus E and Poisson's ratio ν . g is the acceleration due to gravity. Symbols and parameters are defined in Table 2.

2.1 Modular model for the state of stress

We describe the state of stress within the host rock by a stress tensor σ_{ij} . Tensional stresses are positive. σ_{ij} is diagonalized to retrieve magnitudes, $\sigma_1, \sigma_2, \sigma_3$, from most compressive to least compressive, respectively, and eigenvectors, $\vec{v}_1, \vec{v}_2, \vec{v}_3$, which identify the orientations of the principal stress axes.

We build our 3D stress model following the first-order linear approach by Rivalta et al. (2019), who expressed the elastic stress field σ_{ij} of a volcanic region as the superposition of perturbations from a background stress state σ_{ij}^0 , each stemming from a different stress-generating mechanism, according to a first-order linear approach that neglects coupling between the stress sources. We model the stress state of calderas limiting our analysis to tectonic stresses and gravitational loading/unloading because, as dis-

114 cussed by Rivalta et al. (2019), dike patterns can often be explained by a combination
 115 of the two mechanisms, which are in most cases the dominant ones (Gudmundsson, 1995;
 116 Roman & Jaupart, 2014; Corbi et al., 2015; Heimisson et al., 2015; Maccaferri et al., 2017;
 117 Neri et al., 2018). We do not include contributions associated to pressurized magma reser-
 118 voirs, intrusions or strains induced by large earthquakes. This has the advantage of lim-
 119 iting the number of parameters in the model, while retaining the stress mechanisms with
 120 the largest influence. More contributions can be easily added, if needed in specific cases.

121 We write the stress tensor at any point in the crust as:

$$\sigma_{ij}(x, y, z) - \sigma_{ij}^0(z) = \sigma_{ij}^T + \sigma_{ij}^G(x, y, z) \quad (1)$$

122 where the stress terms on the right side arise, respectively, from the regional tectonic stress
 123 (T) and the gravitational loading/unloading (G).

124 The first step in the stress modelling is to define the unperturbed state of stress,
 125 σ_{ij}^0 , before any of the sources on the right hand side of Equation 1 became active. There
 126 are two main assumptions in literature: a laterally-confined medium, that is, no lateral
 127 strain can be produced after gravity is turned on (e.g. Martel & Muller, 2000; Savage
 128 et al., 1985), resulting in a vertical \vec{v}_1 :

$$\sigma_{xx}^0 = \frac{\nu}{(1-\nu)}\rho_r g z, \quad \sigma_{yy}^0 = \frac{\nu}{(1-\nu)}\rho_r g z, \quad \sigma_{zz}^0 = \rho_r g z. \quad (2)$$

129 or a lithostatic stress state:

$$\sigma_{xx}^0 = \sigma_{yy}^0 = \sigma_{zz}^0 = \rho_r g z. \quad (3)$$

130 Field measurements of subsurface stress (Jaeger et al., 2007) lie somewhat in between
 131 those two assumptions. Therefore, σ_{ij}^0 can be written as:

$$\sigma_{xx}^0 = \sigma_{yy}^0 = k\rho_r g z, \quad \sigma_{zz}^0 = \rho_r g z, \quad (4)$$

132 where $k \in [\frac{\nu}{(1-\nu)}, 1]$ (Jaeger et al., 2007; J. R. Muller et al., 2001; Slim et al., 2015).
 133 In this study, we always set $k = 1$ and assume a lithostatic unperturbed stress.

134 The second step is to superimpose the tectonic stress, expressed in terms of three
 135 independent components $\sigma_{xx}^T, \sigma_{yy}^T, \sigma_{xy}^T$, which we assume are uniform (e.g. McKenzie,
 136 1978; Müller et al., 1992).

137 The third step is to consider gravitational stresses associated to surface loading or
 138 unloading. This has often been modeled by distributions of normal forces onto a half-
 139 space: they can be applied to both 2D and 3D problems (Dahm, 2000b; Maccaferri et
 140 al., 2014; Neri et al., 2018), but are inaccurate near the topography, and provide no in-
 141 formation on the stress within the topography itself (McTigue & Mei, 1981). More so-
 142 phisticated analytical solutions exist, but are either 2D (Savage et al., 1985; McTigue
 143 & Mei, 1981) or only for simple topographies (McTigue & Mei, 1987).

144 Martel and Muller (2000) and Slim et al. (2015) described how to implement to-
 145 pographic loads within Boundary Element (BE) models, where the topography is dis-
 146 cretized into a mesh of dislocations. Martel and Muller (2000) considered the effect of
 147 topographic loading as akin to cutting an infinite body subject to gravity in two halves
 148 along a surface defined by the topography. The gravitational stress imposed by the up-
 149 per half onto the lower one is then subtracted from the background stress of the body
 150 (Martel & Muller, 2000, Figure 3). In practice, this is achieved through imposing bound-
 151 ary conditions on the BEs, depending on the coordinate z of their midpoints and the rock
 152 density, which control the overburden or excavation pressure imposed by the topogra-
 153 phy.

154 One important point in models such as Martel and Muller (2000) is that the bound-
 155 ary conditions at the BEs representing the topography are univocally fixed only once the

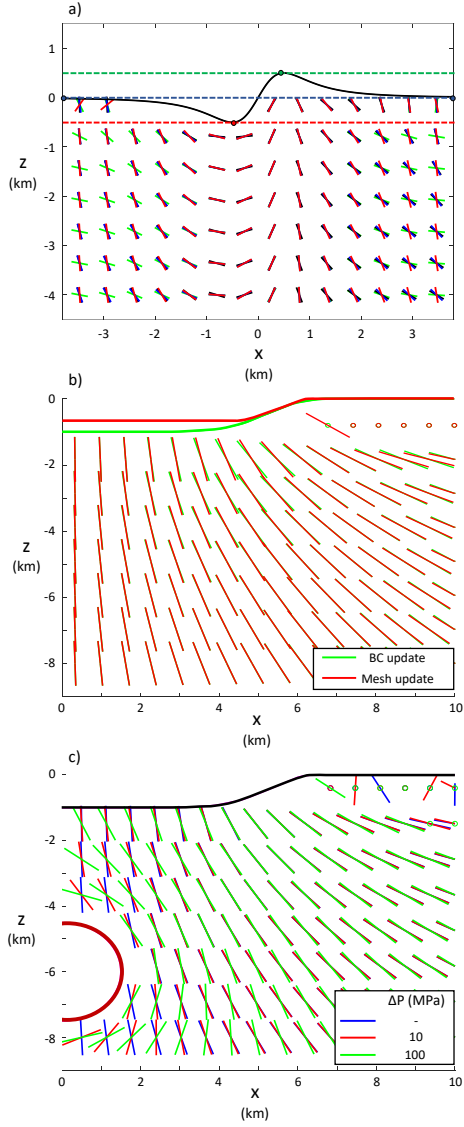


Figure 1. a) Datum level choice: most compressive principal stress orientation due to gravitational loading/unloading of a valley adjacent to a ridge (profile is drawn in black) under plane strain condition. The analytical solution by McTigue and Mei (1981) (black) is compared to our numerical solution with datum level fixed at the flat extremes of the topography (blue), the ridge summit (green) and the valley bottom (red). b) Evolving topography: a 1-km-deep axisymmetric caldera is refilled by 1/3 of its original depth. Least compressive principal stress orientation for two models. Green: the mesh reproduces the caldera before the refilling, and boundary conditions (BC) on the BEs account for the latter. Red: the mesh reproduces the caldera after the refilling. c) Importance of reservoir: least compressive principal stress orientation for three models involving a 1-km-deep axisymmetric caldera and no tectonic stress. Two models include a 6-km-deep spherical magma reservoir of 1.5 km radius, with overpressures $\Delta P=10$ MPa (red) and 100 MPa (green) respectively; one has no reservoir (blue).

156 datum level, that is the unperturbed surface before any topography is created, is set. This
 157 is rarely clarified in applications of similar models (e.g. Chadwick & Dieterich, 1995; Ur-
 158 bani et al., 2017; Neri et al., 2018). Identifying such surface is not always trivial but crit-
 159 ical, as different choices lead to different outcomes for the displacement and stress field.
 160 We show this in Figure 1a, where we compare v_1 from the analytical solution by McTigue
 161 and Mei (1981) for a valley adjacent to a ridge under plane strain assumption to 2D nu-
 162 merical models where the datum level is set to, successively, the flat extremes of the pro-
 163 file, the ridge summit and the valley bottom. The first model shares the same assump-
 164 tion on the datum level with the analytical solution, hence the good agreement for that
 165 case. Such assumption is straightforward to adopt when the topography becomes uni-
 166 formly flat away from the loaded/unloaded region. However, this is not always the case,
 167 and the optimal choice of datum level may depend on the situation. Take e.g. a caldera
 168 lying on a coastline, which divides two regions, the mainland and the sea floor, at dif-
 169 ferent elevations. We consider a similar case in our synthetic scenarios, and we solve the
 170 ambiguity in the datum level by setting it to the ground elevation before the caldera was
 171 formed: this coincides with the sea level in our case. If, for instance, we were to study
 172 the formation of an edifice and, later, of a caldera at its summit, we would first set the
 173 edifice datum level at its base, and then set the caldera datum level at the edifice sum-
 174 mit. Consequently, the topography preceding the reference event (in our scenarios, the
 175 caldera formation) informs the datum level.

176 A further issue regarding the calculation of surface loading/unloading stresses is
 177 that they are not immutable. Volcanic regions host a variety of stress-generating and stress-
 178 relieving mechanisms acting on different time scales (e.g. McGarr & Gay, 1978; Stephans-
 179 son, 1988; Savage et al., 1992; Chadwick & Dieterich, 1995). For example, the build-up
 180 of a volcanic edifice consists of progressive accumulation of eruptive material that loads
 181 and stresses the underlying crust, while, at the same time, magmatic intrusions, earth-
 182 quakes and inelastic processes tend to relax shear stresses and homogenize principal stresses.
 183 Here we avoid this issue by focusing on calderas that we assume have formed relatively
 184 recently in the history of the volcano topography, and consider otherwise only mild to-
 185 pographies, so that modeling dike propagation within edifices is not necessary. We elab-
 186 orate further on this point in Section 4.

187 We compute $\sigma_{ij}^G(x, y, z)$ in Equation 1 following Martel and Muller (2000); Slim et
 188 al. (2015). We employ the 3D BE tool *Cut&Displace* (Davis et al., 2017, 2019), based
 189 on the displacement discontinuity method by Crouch et al. (1983). The topography is
 190 discretized into a mesh of triangular dislocations (Nikkhoo & Walter, 2015), acting as
 191 BEs. The 3D mesh needs to be larger than the region of interest, so that its edges are
 192 distant enough from the volume where we compute the stress. We find that a mesh with
 193 a diameter three times the lateral extent of the studied region is enough for that pur-
 194 pose. If a coastline is present, the outer mesh tapers to two horizontal surfaces at dif-
 195 ferent height, representing the far-field mainland and the far-field sea floor. Once the da-
 196 tum level is fixed, stress boundary conditions are imposed on each BE as we previously
 197 described. The load imposed by the water column on the bathymetry is also included.

198 Calderas are usually filled with eruptive material or sediments over time (e.g. Orsi
 199 et al., 1996; Hildreth et al., 2017). Our model can account for this in several ways: the
 200 buried caldera floor may be meshed as the reference topographic relief, and correspond-
 201 ing BEs may be loaded accounting for the density contrast between the deeper host rock
 202 and the layers above. Alternatively, the current caldera topography may be meshed as
 203 the reference topographic relief, and the unloading pressure resulting from the missing
 204 mass due to lower density infill is factored in the boundary conditions. Calculations for
 205 these options for a synthetic caldera (Figure 1c) show good agreement except in the prox-
 206 imity of the caldera rim. Here we follow the former approach in one scenario, as illus-
 207 trated later.

208 We remark that some of the stress sources we neglect, such as magma reservoirs,
 209 are in principle straightforward to include in our BE model. In order to show the mi-
 210 nor relative influence of such sources, we compare in Figure 1b the orientation of \vec{v}_3 for
 211 three different models: one without and two with a pressurized, spherical magma cham-
 212 ber, with overpressure of 10 MPa and 100 MPa, all involving the same surface unload-
 213 ing and tectonic stress. Only with extremely large overpressures the effects of the pres-
 214 surization are felt at a distance of up 1 source diameter. This validates in 3D a similar
 215 argument by Rivalta et al. (2019) (see their Figure 1).

216 2.2 Three-dimensional dike propagation model

217 2.2.1 Simplified Analytical Model (SAM)

218 Next, we develop a computationally-efficient 3D dike propagation model that pro-
 219 vides a 3D equivalent to 2D \vec{v}_3 -perpendicular streamlines. There is no straightforward
 220 method to compute streamlines in 3D, as the direction of \vec{v}_3 alone identifies a surface,
 221 while the direction of propagation on that surface remains undetermined. Davis et al.
 222 (2020, 2021) developed a pointwise, analytical dike trajectory calculator, similar to Sigmundsson
 223 et al. (2015) but fully 3D and more comprehensive in terms of factors considered. Its pur-
 224 pose was to justify why an observed dike took a specific direction depending on the magma
 225 buoyancy and the external state of stress, and falls short of being a propagation model.
 226 Here we simplify that approach and turn it into a self-propelling 3D propagation model
 227 that can also backtrack dike trajectories downward from a vent to the magma storage
 228 region. We henceforth refer to our model as the ‘Simplified Analytical Model’ (SAM).

229 In the analytical model by Davis et al. (2020, 2021), propagation of the tip-line of
 230 a dike occurs when the local mode I stress intensity factor, K , is larger than the frac-
 231 ture toughness, K_c , of the host rock (e.g. Secor Jr & Pollard, 1975). The dike is repre-
 232 sented as a tensile, penny-shaped crack with a fixed volume, V , and radius, c . It is as-
 233 sumed that external stress varies linearly in every direction over the crack surface, and
 234 that internal pressure varies linearly with z proportional to $\rho_m g \sin \beta$, where β is the crack
 235 dip. In such case, K can be written as:

$$K = \frac{3\mu V}{4(1-\nu)c^2\sqrt{\pi c}} + \frac{4}{3\pi}(\Delta\gamma c\sqrt{\pi c})\cos\alpha, \quad (5)$$

236 (Tada et al., 2000), where α is the angle spanning the circumference of the crack away
 237 from the direction of the maximum linear pressure gradient loading the dike plane, $\Delta\gamma$.
 238 The first term in Equation 5, which depends only on V , determines the magnitude of
 239 K . The second contribution, which accounts for the effect of $\Delta\gamma$, determines the angle
 240 α for which K is maximum, and thus the direction of propagation of the crack. If $R_K =$
 241 $K/K_c > 1$, the crack is expected to propagate (see Figure 1 in Davis et al., 2020).

242 In SAM, we simplify such approach by, first, assuming that the dike opens against
 243 the local \vec{v}_3 , calculated from the stress model defined in Section 2.1, and is represented
 244 as a penny-shaped crack with fixed radius c . Secondly, we calculate K as

$$K = \frac{4}{3\pi}(\Delta\gamma c\sqrt{\pi c}). \quad (6)$$

245 This is equivalent to neglecting the role played by the dike volume and K_c in determin-
 246 ing whether the dike will advance. On the other hand, the buoyancy force contributes
 247 to $\Delta\gamma$ in SAM, and plays a role in determining the direction of propagation on the \vec{v}_3 -
 248 perpendicular surface.

249 We use a Cartesian reference frame, where the z -axis is positive upward (Figure 2a).
 250 We later employ a cylindrical reference frame to identify the starting points of dikes (Fig-
 251 ure 2a) where the radial distance from the origin is indicated as r and the angle mea-
 252 sured counterclockwise from the positive x -axis is indicated as ϕ .

253 We calculate forward dike trajectories (FTs) as follows:

- 254 1. We produce a stress model for the hosting medium (section 2.1).
- 255 2. We choose a starting point F_0 for the dike (for instance, at the edge of a magma
256 reservoir).
- 257 3. We compute σ_3 and \vec{v}_3 at F_0 and identify the local surface Σ perpendicular to \vec{v}_3 .
258 The dike is then defined as a penny-shaped crack of radius c lying on Σ (Figure 2a).
- 259 4. We compute K along the dike's tip-line. To do so, we generate a ring of n regularly-
260 spaced observation points O_i , $i = 1 \dots n$ at a distance c from F_0 (Figure 2b).
- 261 5. We calculate σ_3^i at each O_i and use it in place of the normal stress to calculate
262 $\Delta\gamma$ for every point on the ring as:

$$\Delta\gamma_i = \frac{(\sigma_3^i - \sigma_3^j)}{2c} - \rho_m g \frac{(z_O^i - z_O^j)}{2c}, \quad (7)$$

263 where z_O^i , z_O^j are the vertical coordinates of points O_i , O_j , with O_j antipodal to
264 O_i .

- 265 6. We calculate K^i at each O_i according to Equation 6 and determine the point F_1
266 where $K^i = K^{max}$. This will identify the direction of propagation of the dike (Fig-
267 ure 2b).

268 We reiterate the previous steps taking F_1 as the current F_0 . This will produce a
269 chain of points identifying the trajectory of the dike. The dike stops once at least one
270 of the observation points generated in step 3 reaches the free surface. The center of the
271 current Σ is then taken as the arrival point F_A (Figure 2b). In our stress models, how-
272 ever, a further issue emerges. In general, a minimum distance threshold (MDT) needs
273 to be maintained between the observation points and the mesh, in order to prevent ar-
274 tifacts singularities in the stress calculations (Slim et al., 2015). This is a characteris-
275 tic issue of BE models, and can be mitigated with finer meshing, or aligning the obser-
276 vation points to the midpoints of the BEs (Slim et al., 2015). Due to this issue and to
277 the finite size of the BEs representing the free surface, we do not allow dikes to proceed
278 beyond a certain distance from the free surface. Here we fix the MDT to 800 m away
279 from the nearest BE, as this is the average size of the dislocations of the mesh we em-
280 ploy. Dikes may be propagated past their F_A until they hit the surface at a 'projected'
281 arrival point, F_A^P , assuming that they maintain the dip and strike calculated at F_A (Fig-
282 ure 2b). This is akin to assuming that dikes do not have the space to adjust to the lo-
283 cal stress field in the last 1 km before reaching the free surface. A SAM dike is forced
284 to stop if the trajectory becomes horizontal, or if the difference in the strike and dip an-
285 gles between the current direction of propagation and the one at the previous step is larger
286 than a given threshold. This prevents abrupt turning in the dike pathways.

287 SAM trajectories depend on two parameters, c and n . We found that values of n
288 equal or greater than 12 lead to nearly identical dike pathways; we set n to 12 in all sce-
289 narios calculated later. In contrast, different c lead to different trajectories and arrival
290 points for the same starting points and stress field. Large c (e.g. > 2 km if the dike start-
291 ing point is 10 km deep) sample the stress field in too few points and do not produce ac-
292 curate trajectories, while very small c (e.g. < 50 m for the starting depth mentioned above)
293 are computationally expensive and follow principal stress directions nearly pointwise, as
294 streamlines do in 2D. In this perspective, c controls how much SAM trajectories devi-
295 ate from the stress directions. We show later how c may be calibrated to better match
296 a more sophisticated dike propagation model.

297 SAM also allows for the propagation of anti-buoyant dikes, that is, dikes filled with
298 $\rho_m > \rho_r$ propagating downward through the crust. Dike trajectories, however, cannot
299 be backtracked by simply inverting the density contrast between magma and rocks: an
300 anti-buoyant dike starting from the arrival point of a buoyant one and propagating down-
301 ward with the same c and n will not pass through the same points (see Figure 2c), even

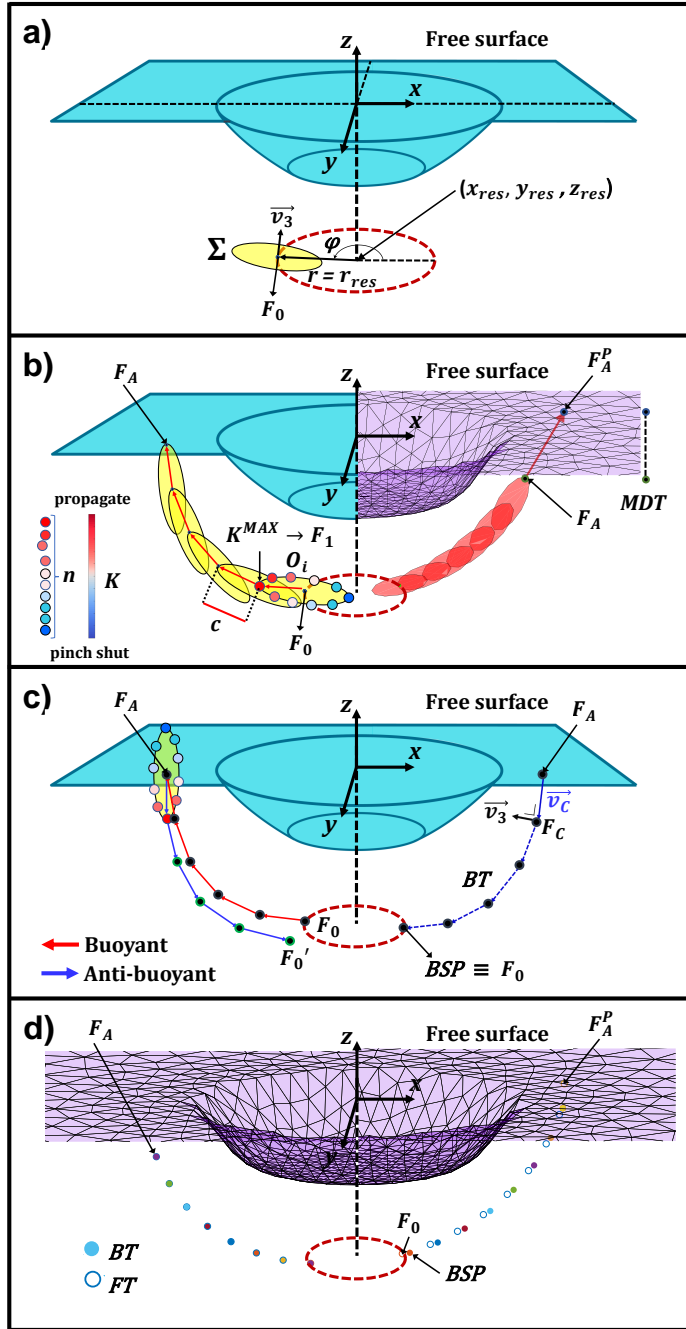


Figure 2. SAM framework. a) reference systems employed throughout the work and notation for the dike radius and starting point. Blue surface: simplified topography with a circular caldera. Red dotted line: edge of a magma storage region where the dike departs. Yellow surface: dike's initial opening surface (Σ). b) Left: full SAM trajectory, arrival point and detail of first step of the algorithm. Colored dots: observation points O_i ; the colors are associated to K according to the colorbar. Right: BE mesh of the topography (vertically exaggerated) and actual FT from scenario STC-3 (see Section 2.3), extended until the free surface. Black dotted line on the right: MDT (here set to 2 km). c) Backtracking of SAM trajectories. Left: comparison between buoyant (red) and anti-buoyant (blue) trajectories. Right: representation of the backtracking algorithm outlined in Section 2.2. d) Backtracked trajectories (BTs) of the forward trajectory (FT) shown in b). Left: BT starts from the actual arrival point. Right: BT starts from the projected arrival point. Colored dots on both sides represent the BTs; empty blue dots the original FT.

if, as we observed, the difference between forward trajectories (FTs) and backtracked trajectories (BTs) decreases for smaller values of c .

We backtrack FTs, from known arrival points F_A and with assumed parameters c_B and n_B , as follows:

1. Starting from F_A , we find a candidate point B_C at a distance c_B such that the scalar product between \vec{v}_3 at B_C and the vector \vec{v}_C pointing from B_C to F_A is minimal (Figure 2d).
2. We run one step of the forward model from B_C and calculate the vector between the predicted and actual F_A ; we then shift B_C by that same vector and iterate this procedure until the desired precision is attained, and B_C is taken as the first point B_1 of the BT.
3. The algorithm stops as soon as a specific requirement is satisfied: for instance, the current B_j falls within the known magma storage region. The lastly-recovered point of the BT becomes then the "backtracked starting point" (BSP) (Figure 2d).

The first step of the algorithm is modified when starting from F_A^P lying on the free surface, as we no longer fix the distance between B_C and F_A^P to a specific c_B , but let it vary over a specific range (for a FT with given c , we find a $0-3c$ range enough for our purpose).

We tested the method against known forward trajectories, and found that it is able to retrieve each F_0 within a range of a few tens of meters if starting from F_A , and a few hundreds if starting from F_A^P , provided the same radius c of the forward model is employed ($c_B = c$). If that is not the case, the distance between actual and backtracked starting point ($\Delta_{BSP} = |F_0 - BSP|$) increases with the difference between the back-track radius c_B and c .

2.2.2 Three-dimensional Intrusion Model (TIM)

We later validate SAM against a more sophisticated dike propagation model. To this end, we employ the numerical, full-3D dike propagation model by Davis et al. (2020) and Davis et al. (2021). The model needs the dike volume (V), assumed constant during the propagation, and the magma density (ρ_m). The dike starts as a penny-shaped crack centered at a specific starting point and arranged according to a starting dip and strike; these can be either arbitrary or coincide with the local \vec{v}_3 . The dike starting radius is then taken as $c_0 = \sqrt{V/1.6\pi}$. The dike is discretized into a mesh of triangular dislocations, and R_K is computed at every BE lying on the dike tip-line (Davis et al., 2019); the tip line is advanced or retreated by an amount proportional to the local R_K , depending on its sign, and the crack is remeshed. The crack can also bend out of its plane according to the maximum circumferential stress criterion (Pollard et al., 2005; Davis et al., 2021). The dike can thus advance along complex trajectories and change its shape in the process. As such, the model captures the effect of dike volume and buoyancy as well as the external stress. In the following, we refer to it as 'Three-dimensional Intrusion Model' (TIM).

Before comparing TIM and SAM trajectories, we illustrate how to combine the stress and dike models introduced so far into synthetic scenarios of dike propagation.

2.3 Setup of dike propagation scenarios

We start by producing a stress model for a given caldera. In a real case, we first evaluate which stress mechanisms are most relevant. Here, as discussed in Section 2.1, we limit our analysis to tectonic stresses and gravitational loading/unloading. We calculate the latter as described in Section 2.1, and we superimpose to the resulting stress field the tectonic stress components σ_{ij}^T .

Table 1. Parameters of the dike propagation model.

Symbol	Description	Units
Host rock density	ρ_r	kg/m ³
Magma density	ρ_m	kg/m ³
Host rock fracture toughness	K_C	Pa√m
Young's modulus	E	Pa
Poisson's ratio	ν	
Forward dike trajectory	FT	
Dike starting point	F_0	
Dike radius	c	m
Dike surface	Σ	
Number of observation points along the dike tip-line	n	
Observation points	$O_i, i = 1, \dots, n$	
Dike arrival point	F_A	
Points defining dike trajectory	$F_i, i = 1, \dots, A-1$	
Projected dike arrival point	F_A^P	
Backtracked dike trajectory	BT	
Backtracked dike radius	c_B	m
Points defining backtracked trajectory	B_i	
Backtracked dike starting point	BSP	

349 We fix the location of the magma reservoir, which will constitute the rock volume
350 where dikes depart from. Dike starting points are described by z_0^k , radius r_0^k and angle
351 ϕ_0^k , $k = 1, \dots, N$ (Figure 2a). In simplified scenarios, we fix equally-spaced starting points
352 along the edge of circular, sill-like reservoirs. In more complex scenarios, starting points
353 are generated from a probability distribution in z , r , ϕ that quantifies our uncertainty
354 on the favored dike nucleation sites around the reservoir.

355 As a final step, we choose a model of dike propagation and define the needed input.
356 TIM needs dike volumes (V^k), magma densities (ρ_m^k), K_c of the host rock and a
357 starting geometry for the k -th dike. Starting dike radii are fixed as $c_0^k = \sqrt{V^k/1.6\pi}$ (see
358 Section 2.2 and Davis et al., 2021). SAM needs c and ρ_m : here, they are the same for
359 all dikes in each scenario.

360 We produce a total of eight synthetic scenarios, referred to as STC- i , $i = 1, \dots, 8$
361 (Tables 2 and 3). We fix the Young's modulus and Poisson's ratio of the medium to $E =$
362 15 GPa and $\nu = 0.25$, respectively. The fracture toughness of the host rock is fixed to
363 $K_C = 70 \text{ MPa}\cdot\text{m}^{1/2}$. The densities of the host rock (ρ_r) and the magma filling the dikes
364 (ρ_m) are set as in Tables 2 and 3.

365 We consider increasingly complex topographies with an approximately circular or
366 elliptic caldera located at the origin of the cartesian reference frame (see Figure 2a). A
367 resurgent dome may also be included, as well as a coastline and/or hills. We employ four
368 main topographic settings, each corresponding to one or more scenarios:

- 369 1. Setting 1 (STC-1,3): a flat topography with a circular caldera of radius $R_C = 6$
370 km and maximum depth $d = 500$ m. The depth of the caldera, which has steep
371 slopes and a flat floor, varies with r according to:

$$z = \exp(-r^6) \quad (8)$$

- 372 2. Setting 2 (STC-4,5): we add a coastline to the flat topography from (1), modelled
 373 as a steep elevation step along the y -axis. The bathymetry lies 100 m below the
 374 datum level. The caldera has $R_C = 6$ km, $d = 450$ m, and depth varying with
 375 r as in (1).
- 376 3. Setting 3 (STC-2,6,7): we maintain the bathymetry of (2), but we include two hills
 377 (heights 791 m and 355 m, base diameter ~ 15 km). The caldera has $R_C = 6$ km
 378 and maximum depth $d = 424$ m. The caldera shape is made irregular by adding
 379 Gaussian noise to Equation 8. In STC-6 we model a topography evolving from set-
 380 ting (3) to (3b), where the caldera is partially refilled, with its maximum depth
 381 changing to $d = 221$ m.
- 382 4. Setting 4 (STC-8): an elliptic caldera with $d = 150$ m, semi-major and semi-minor
 383 axes $a_C = 8$ km and $b_C = 4$ km, respectively. A circular resurgent dome with
 384 $h = 150$ m and 4.8 km diameter is located 3 km offset from the caldera center.
 385 The external topography has some gently-sloping hills (the maximum height is 157
 386 m), but no bathymetry.

387 All scenarios involve tensional stresses, whose principal axes coincide with the co-
 388 ordinate axes except for STC-5.

389 For all scenarios except for STC-2,7,8 dikes nucleate at same depth $z_0^k = z^{\text{res}}$ and
 390 radius $r_0^k = r^{\text{res}}$ (see Table 3 for numerical values). In STC-2, we include a starting point
 391 at a radius larger than r^{res} . Two different nucleation depths and radii are considered in
 392 STC-7. In STC-8, z_0^k are drawn from a beta distribution skewed towards the upper edge
 393 of the reservoir (see Figure 5f). STC-1 has only one starting point. ϕ_0^k are equally-spaced
 394 in STC-2,3,4,5 and drawn from a uniform distribution in STC-7,8. All nucleation vol-
 395 umes are centered at the origin of the cartesian reference frame, except for STC-8, which
 396 is centered below the summit of the resurgent dome. We remark that here these ‘reser-
 397 voirs’ where dikes depart from have no contribution to the stress field.

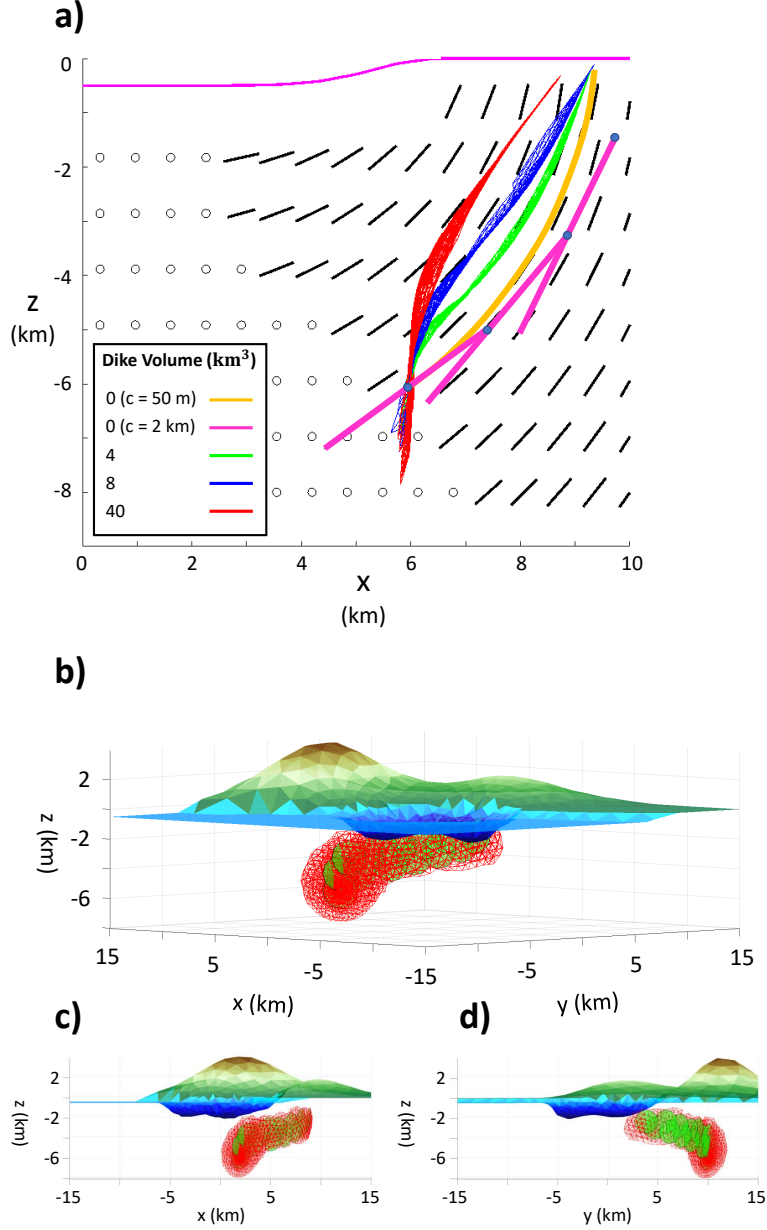


Figure 3. TIM and SAM comparison. TIM pathways: series of meshes representing a subset of steps in dike propagation. Starting and final configuration of dikes are always included. Triangular dislocations are shown as red, empty triangles. a) In scenario STC-1, two SAM dikes with different c compared to to three TIM dikes with the same magma density and increasingly larger volumes. All dikes start from $x = 6$ km, $y = 0$ km, $z = -6$ km; dikes are vertically-oriented at the starting point. Black segments show \vec{v}_1 projected over the x - z plane; black circles represent out-of-plane \vec{v}_1 . Topography is represented as a magenta line. Blue dots mark the actual trajectory of SAM dike with largest c . b) In scenario STC-2, perspective view of first TIM dike and associated SAM dike propagating laterally beneath a topographic high. Both dikes start from ($x = 2$ km, $y = 10$ km, $z = -6$ km), aligned to local \vec{v}_3 . c) Side view of b) along x -axis. d) Side view of b) along y -axis. For host rock and magma properties see Table 2.

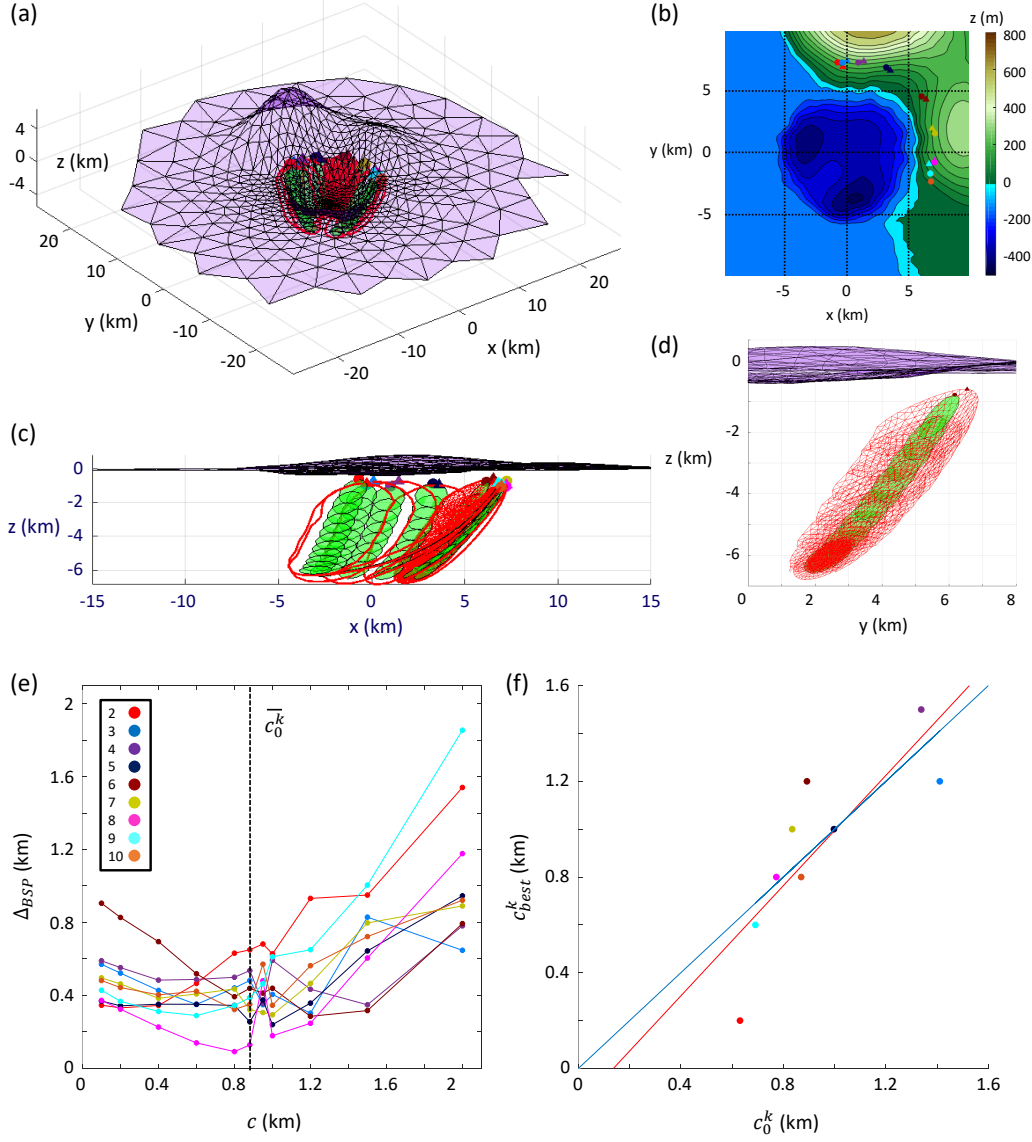


Figure 4. STC-2 scenario: TIM and SAM comparison. Only outlines of TIM pathways are shown, except for the fifth dike, shown as a series of steps in the simulation as in Figure 3. a) synthetic topography with a vertical exaggeration factor of 10. b) elevation map and arrival points of TIM (triangles) and SAM (dots) dikes. Each dike is associated to a fixed color. c) side view of topography, TIM (red) and SAM (green) pathways, dike starting and arrival points. TIM pathways are outlined except for the fifth dike, where we display the BE mesh. d) detail of TIM and SAM pathways for the fifth dike. Triangular dislocations in TIM are visible as red, empty triangles. e) SAM backtracking method applied to TIM pathways; distance between the actual and backtracked starting point Δ_{BSP} versus c . Black dotted line marks the average of c_0^k of TIM dikes. Colors correspond to dikes as in b) and c), and are associated in the inset to STC-2 dikes in Table 2. f) c_{best}^k : c yielding the smallest Δ_{BSP} versus starting dike radius for each dike. The red line fitting the data is compared to the bisector (blue line).

Table 2. Parameters of TIM dikes in STC-1 and STC-2.

Dike	V_k $\cdot 10^6 \text{ m}^3$	c_0^k km	ρ_m^k kg/m ³
STC-1			
1	4	0.89	2300
2	8	1.26	2300
3	40	2.82	2300
STC-2			
1	4	0.89	2700
2	2	0.63	2300
3	10	1.41	2250
4	9	1.34	2100
5	5	0.99	2280
6	4	0.89	2350
7	3.5	0.83	2300
8	3	0.77	2270
9	3.8	0.87	2390
10	2.4	0.69	2300

2.4 SAM and TIM comparison

We now proceed to validate SAM against TIM to assess under which conditions the two models are compatible and, in particular, how a proper calibration of c allows SAM to match TIM pathways, both in forward and in backward. In particular, we want to test the hypothesis that the c leading to the best match between SAM and TIM dikes may coincide with their starting radius ($c = c_0$) or, if multiple TIM dikes are present, the average of their starting radii ($c = \bar{c}_0^k$).

We use STC-1, which offers the simplest topography, and STC-2, which offers the most complex one, to compare TIM and SAM and to calibrate c . For TIM dikes, we fix volumes (V^k), starting radii (c_0^k) and magma densities (ρ_m^k) as in Table 2. In STC-1 (Figure 3a), we show a situation where the two models diverge. We run three TIM dikes with different V^k and two SAM dikes with different c , propagating from the same starting point and with the same ρ_m . While TIM dikes start with an arbitrary, vertical orientation, SAM dikes have to start perpendicular to \vec{v}_3 . This leads to very different pathways between SAM dikes and TIM dikes. From Figure 3a, it is evident how TIM dikes with larger volumes require larger distances to adjust to the stress directions, as already captured in 2D models (Dahm, 2000a; Maccaferri et al., 2010). We also notice how the SAM dike with the smallest c follow the stress field more closely. Thus, SAM and TIM dikes converge to the same trajectory only if the latter start already oriented to the external stress or, alternatively, if SAM dikes start where TIM ones have adjusted to it.

In STC-2 we show a situation where SAM dikes capture 3D propagation as well as TIM dikes. In Figure 3b,c,d, we run a TIM dike starting beneath a topographic high, and compare it to a SAM dike starting from the same point. In this model, we set both dikes to be weakly buoyant ($\rho_r - \rho_m = 100 \text{ kg/m}^3$) and start already aligned to the local stress directions. They both propagate laterally along similar trajectories, as dictated by the external stress and the low magma buoyancy: such behavior may not be captured by 2D dike models. We find that the SAM dike fits the TIM pathway best if we take $c = c_0^1$, that is the starting radius of TIM dike (Table 2). In Figure 4a,b,c,d, we run additional nine TIM dikes with different V^k , c_0^k and ρ_m , and compare them to

427 forward SAM trajectories. Despite the V^k , c_0^k and ρ_n^k being different from one dike to
 428 another, the arrival points and final orientations of the SAM dikes are consistent with
 429 the outcomes of the TIM dikes, and SAM trajectories follow closely TIM ones. We find
 430 that such match is closest when we take $c = \bar{c}_0^k$, that is, the average of the c_0^k .

431 We also backtrack the nine TIM dikes with SAM, and evaluate how accurately their
 432 starting points are recovered with different values of c_B (Figure 4e,f). The BTs start from
 433 the TIM arrival points and stop once the lastly-retrieved point goes past z^{res} (here as-
 434 sumed known). We find that the performance of our backtracking method in recover-
 435 ing the SP of the TIM dikes depends on the c we employ. Both large (> 1.2 km) and
 436 small (< 0.6 km) c perform poorly. On the other hand, we see in Figure 4e how the dis-
 437 tance between actual SP and BSP of each dike, Δ_{BSP} , is smallest for c equal or close
 438 to $\bar{c}_0^k = 880$ m (black vertical line in Figure 4e). The minimum of Δ_{BSP} for all dikes
 439 except for the one with the smallest V^k (Table 3) is found in the range $600\text{m} \leq c \leq$
 440 1km .

441 In Figure 4f, we plot c_0^k versus c_{best}^k , that is, the c leading to the most accurate BSP
 442 for the k -th dike. We find that the best-fit line comes close to the bisector of the quad-
 443 rant and, thus, $c = c_0^k = \sqrt{V^k}/1.6\pi$ provides a good estimate for the optimal c in SAM.

444 In summary, SAM provides trajectories close to TIM dike trajectories only when
 445 the latter are well-oriented within the external stress field. Then, the optimal c for SAM
 446 may be chosen on the basis of the volumes of TIM dikes. The implication is that, in a
 447 real scenario, knowledge on the volume of actual dikes could inform the choice of c for
 448 both forward and backward SAM.

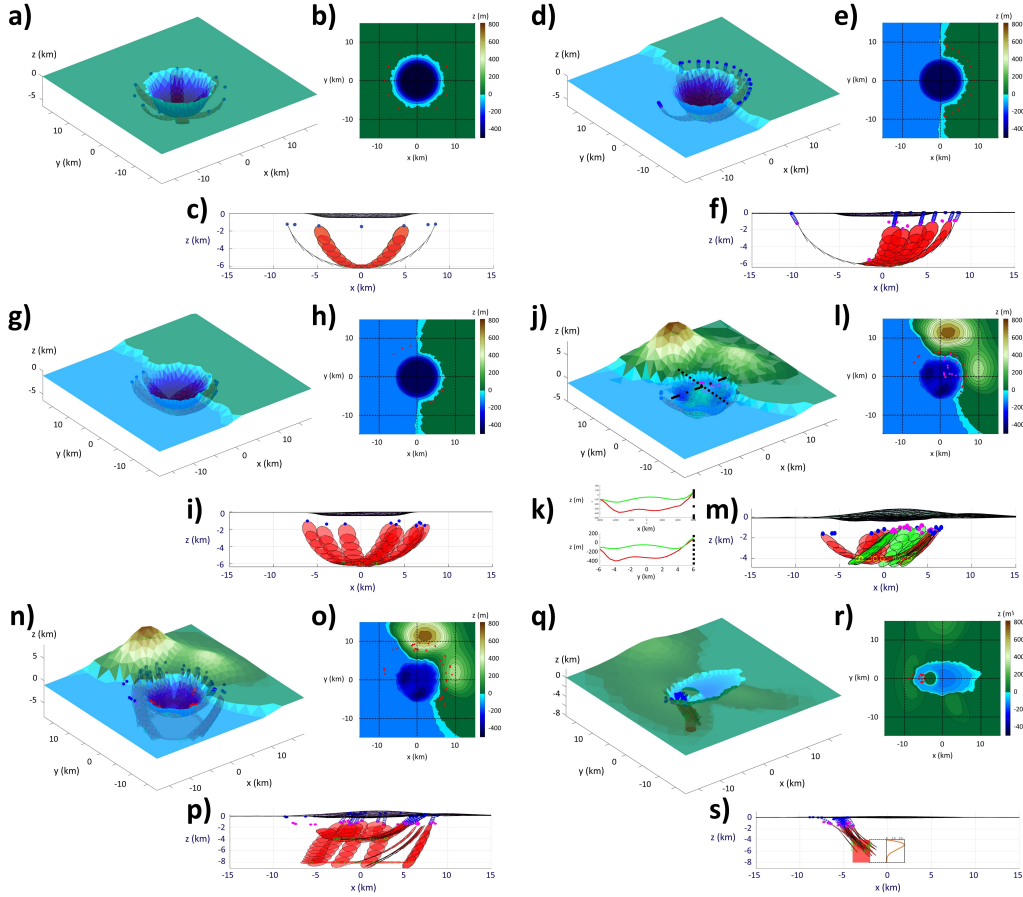


Figure 5. Topography and selected SAM dike trajectories for scenarios STC-3 to STC-8. a), b), c) STC-3: respectively, synthetic topography and dike trajectories, elevation map and dike arrival points, side view of topography and dike trajectories. d), e), f) STC-4: respectively, synthetic topography and dike trajectories, elevation map and dike arrival points, side view of topography and dike trajectories. g), h), i) STC-5: respectively, synthetic topography and dike trajectories, elevation map and dike arrival points, side view of topography and dike trajectories. j), k), l), m) STC-6: respectively, synthetic topography (original and updated) with two cross-sections along x (dots and dashes) and y (fine dots) axes and dike trajectories (red ones run with original topography, green ones with updated topography), topographic profiles along cross-sections in j) showing original (red) and updated (green) topography, elevation map and dike arrival points, side view of topography and dike trajectories. n), o), p) STC-7: respectively, synthetic topography and dike trajectories, elevation map and dike arrival points, side view of topography and dike trajectories. q), r), s) STC-8: respectively, synthetic topography and dike trajectories, elevation map and dike arrival points, side view of topography and dike trajectories with inset showing the probability distribution from which vertical coordinates of dike starting points are drawn. General conventions as follows. Topography in a), d), g), j), n), q) has a vertical exaggeration factor of 10. Dike starting and arrival points are represented as green circles and blue dots (red in elevation maps), respectively. In d), f), n), p), q), s) last points of dike trajectories in subsurface are magenta dots and blue circles are steps of projected dike trajectories to free surface. Magma storage regions: light-red volumes.

Table 3. Chosen topography, tectonic stress, host rock and reservoir parameters of the synthetic scenarios.

# Scen.	d	h	σ_{xx}^T	σ_{yy}^T	σ_{xy}^T	ρ_r	r^{res}	z^{res}
	m	m	MPa	MPa	MPa	kg/m ³	km	km
STC-1	500	-	1	0	0	2500	6	6
STC-2	424	-	1	0.4	0	2800	10.2	6
							3	6
STC-3	500	-	1	0.5	0	2500	2	6
STC-4	450	-	1	1	0	2500	2	6
STC-5	450	-	0.8	0.8	-1	2500	2	6
STC-6	424	-	1	0.4	0	2800	3	4
	221							
STC-7	424	-	1	0.4	0	2800	3	4
							6	8
STC-8	150	150	1	0.6	0	2500	1	6

3 Results

In scenarios STC-3 to STC-8, we use SAM to produce dike pathways and vents (Figure 4). FTs are stopped at the distance threshold from the BEs in STC-3,5,6. Conversely, FTs are propagated past that threshold in STC-4,7,8 according to the method explained in Section REF. STC-4,7,8 are thus the only scenarios where surface vents are produced.

The simplest model is STC-3 (Figure 5a,b,c), where the caldera is an axisymmetric, circular depression on a flat surface. Here, dike trajectories are deflected by the gravitational unloading associated to the caldera, and their arrival points punctuate its rim. The tectonic extension is higher along the x -axis, and this leads to the spacing between neighboring arrival points becoming smaller when closer to that axis, even if the starting points are equally spaced.

STC-4 (Figure 5d,e,f) presents a more complex topography, where a simplified caldera lies on a coastline between two flat regions at different heights. This has an evident impact on dike trajectories, which are still deflected away from the caldera, but end up mostly on the mainland. Only the dike starting farthest away from the mainland manages to reach the sea floor. In particular, there is a concentration of arrival points close to the coastline. The effect of deviatoric tectonic stress is most apparent in STC-5 (Figure 5g,h,i). Here, the least-compressive principal tectonic stress axis roughly strikes along the bisector of the second and fourth quadrants (respectively, negative x -axis and positive y -axis, and viceversa). Arrival points cluster about such axis, both on the mainland and on the sea floor.

STC-6 (Figure 5j,k,l,m) considers two different topographies. The first, associated to the red dike set, is the same as STC-2. Dikes are deflected away from the caldera and punctuate its rim on the mainland. Three dikes reach the sea floor. Topographic loads associated to the hills in the first quadrant also tend to attract dikes. The second topography, associated to the green dike set, envisions a partial refilling of the caldera, with a resurgent dome at its center (see Figure 5k). The topography outside the caldera rim is unchanged. Dikes are still deflected by the caldera unloading and focus towards the mainland, but all reach the surface along or within the caldera rim, some ending up on the resurgent dome. We remark that also in STC-2 both TIM and SAM dikes are deflected toward the mainland and along the rim of the caldera (Figure 4a,b,c,d). Even the

480 dikes starting from the sea side of the reservoir end up on the mainland. Dikes that prop-
 481 agate in the proximity of the hills are also deflected towards them.

482 STC-7 (Figure 5n,o,p) shares the topography of STC-2, but includes two different
 483 dike nucleation depths and radii. Dike trajectories show the same pattern as in the pre-
 484 vious scenario, the ones starting from the deeper nucleation region reaching the surface
 485 farther away from the caldera.

486 Dikes in STC-8 (Figure 5q,r,s) feel the competing influence of the elliptic caldera
 487 and the loading due to the resurgent dome and the hill on the left. The synthetic vents
 488 cluster in two areas, the larger adjacent to the dome and the minor close to the caldera
 489 rim and the hill. No vents are present at the top of the dome.

490 In summary, topography plays a dominant role in controlling dike pathways in our
 491 scenarios. Even short-wavelength topographic features, such as a ~ 5 -km-wide resur-
 492 gent dome in STC-8 (Figure 5r), influence close trajectories over a distance compar-
 493 able to their width, e.g. the resurgent dome diameter in STC-8. In all scenarios, dikes are
 494 consistently deflected away from surface unloading and attracted by surface loading. Tec-
 495 tonic stress also influences dike orientation and clustering of arrival points, with a more
 496 evident impact in the simplest scenarios (STC-3,4,5).

497 4 Discussion

498 We have shown how our newly-developed ‘elementary’ dike propagation model (SAM)
 499 well reproduces trajectories calculated with a sophisticated numerical model (TIM) by
 500 Davis et al. (2020, 2021) (Figures 3b, 4), and can effectively model 3D dike pathways in
 501 synthetic calderas with tectonic stress and mild surface loading/unloading (Figure 5).
 502 In particular, SAM and TIM trajectories are similar only if dikes in the latter model start
 503 optimally-oriented to the external principal stress directions (Figure 3a). Dike propa-
 504 gation in both models is controlled not only by the gradients of external stress, but also
 505 by magma buoyancy. SAM is also able to backtrack dike trajectories from a vent to the
 506 magma storage region.

507 Due to our simplifying assumptions, our models have many potential limitations.
 508 The assumptions include homogeneous elastic parameters for the host rock. Rigidity and
 509 density layering may substantially affect dike propagation. For instance, dike trajec-
 510 tories can be deflected when crossing interfaces between layers with strong rigidity con-
 511 trasts, as shown in 2D by Maccaferri et al. (2010). Similar studies are needed to grasp
 512 the effects of layer interfaces in 3D. As shown by Mantiloni et al. (2021) through anal-
 513 og experiments, homogeneous models well reproduce the observed pathways provided
 514 that ‘effective’ stress parameters are employed, rather than those actually imposed on
 515 the gelatin. In this perspective, our simple models will be of advantage in future real-
 516 time or statistical applications, where fast computation is required.

517 We also assume linear elasticity. Volcanic regions are known to host inelastic pro-
 518 cesses such as seismicity, damage, thermoplasticity, infiltration of and alteration by hy-
 519 drothermal and magmatic fluids, that can affect both stresses and dike propagation. In
 520 particular, these inelastic processes compete with stress-generating mechanisms by ho-
 521 mogenizing stresses (e.g. McGarr & Gay, 1978; Stephansson, 1988; Savage et al., 1992).
 522 Repeating magmatic intrusions (e.g. Dieterich, 1988; McGuire & Pullen, 1989; Ventura
 523 et al., 1999; Walter et al., 2005) may also bring the state of stress to isotropic in the long
 524 run: since they tend to open perpendicularly to \vec{v}_3 , the strain they cause tends to bring
 525 σ_3 closer to σ_1 (Chadwick & Dieterich, 1995; Bagnardi et al., 2013; Corbi et al., 2015, 2016).
 526 Additionally, faulting and earthquakes may dissipate shear stresses over time. Thus, the
 527 stress contributions in Equation 1 are not immutable. An accurate calibration of the stress
 528 state needs to take into account the relaxation of each stress contribution over time and
 529 space, discriminating between stress sources (in particular topography-altering events)

530 that became active at different times. For instance, Maccaferri et al. (2017) explored the
531 interplay between the loading stress due to the growth of a volcanic edifice, that dissi-
532 pates over time, and the ‘instant’ stress change due to flank collapse in controlling erup-
533 tive vent patterns, showing how the latter can deflect dike pathways and lead to the for-
534 mation of new eruptive centers. These processes are difficult to constrain and are cur-
535 rently accounted for through approximations. For instance, some works set the devia-
536 toric stresses arising from gravitational loading of the edifice to zero (Heimisson et al.,
537 2015; Davis et al., 2021), arguing that they would be compensated by faulting and dike
538 intrusions over the history of the volcano. Corbi et al. (2015) found that superposing the
539 effect of caldera unloading to a volcanic edifice where the state of stress is set to isotropic,
540 rather than fully loaded, explained much better the orientation of eruptive fissures at
541 Fernandina, Galapagos. Here we neglected such processes by creating scenarios where
542 dikes propagate below and around a caldera but not within an edifice. We tested that
543 accounting for shear stress dissipation and stress homogenization in such scenarios still
544 leads to dike trajectories being deflected by surface unloading and attracted by surface
545 loading. We postpone the study of scenarios that involve propagation within an edifice
546 to a future study.

547 As we show in Figure 1c, stress contributions of magma reservoirs are dominant
548 only in the proximity of the stress source. Such effect, nonetheless, can be important in
549 determining nucleation points for dikes (Gudmundsson, 2006; Grosfils et al., 2015), that
550 we do not model precisely here, as well as attracting or repelling incoming dikes if the
551 reservoir pressure is increasing or decreasing, respectively (Pansino & Taisne, 2019).

552 Stress contributions due to previous large earthquakes may also deviate dikes or
553 arrest their propagation. This has been considered both through theoretical (Maccaferri
554 et al., 2014, 2016) and analog (Le Corvec et al., 2013) modeling. The fault-generated stresses
555 do not influence dike trajectories significantly unless they come to close proximity and,
556 thus, can hardly reproduce observed dike patterns alone (e.g. Maccaferri et al., 2014).
557 However, Maccaferri et al. (2016) showed how a pre-stressed fault can effectively stop
558 dike propagation if a dike hits it at a sub-perpendicular angle. This is due to the stress
559 induced by the approaching dike, which leads to the fault slipping and, in turns, induces
560 compressive stress at the dike’s tip, arresting it. Faults and dikes may also interact with
561 each other, for instance alternately accommodating tectonic extension (Gómez-Vasconcelos
562 et al., 2020).

563 Lastly, the emplacement of dikes affects the local stress field as well, as both an-
564 alytical (Rubin & Gillard, 1998) and numerical models (Ito & Martel, 2002) have shown.
565 The interaction between previous and subsequent intrusions has been suggested as a driv-
566 ing factor in controlling dike trajectories (e.g. Kühn & Dahm, 2008) or recurring dike
567 patterns (e.g. Takada, 1997), and dictating the architecture of reservoirs formed by dis-
568 crete intrusions (Ferrante et al., 2022), while others have stressed the importance of the
569 cumulative effect of repeating dikes on the state of stress at volcanoes (e.g. Cayol & Cor-
570 net, 1998).

571 All these stress sources can be integrated in our models as they stand now. Includ-
572 ing stress mechanisms that are not well-constrained, however, ultimately adds more un-
573 certainty to a model rather than improve it. Thus, in a real scenario, it is more bene-
574 ficial to include only the stress sources that are most relevant and well-known.

575 In our scenarios, dike pathways must stop at a given MDT before reaching the sur-
576 face (See Section 2.2). The MDT we set is compatible with the distance at which dike
577 interaction with the free surface becomes significant (Pollard & Holzhausen, 1979). Sur-
578 face deformation induced by the incoming dike may cause graben faulting to occur (e.g.
579 Hjartardóttir et al., 2016; Xu et al., 2016), thereby relaxing stresses and inducing the
580 dike to stop before reaching the surface. This aspect is important, and may be included
581 in future models.

582 Many dikes in our tests stop before reaching the surface. This happens in both mod-
 583 els when the interplay between the buoyancy force and the external stress gradients is
 584 no longer sufficient to drive the dike upward, and is often associated to gravitational load-
 585 ing (topographic highs). This is shown specifically in Figure 3b, where TIM and SAM
 586 dikes stop and spread laterally beneath a topographic load. In scenarios STC-6,7 we also
 587 notice how dikes ascending below steep hills often stop before reaching the MDT. Ana-
 588 log models (e.g. fluid-filled cracks propagating in gelatin, as in Kervyn et al., 2009), may
 589 further validate such conclusions. Dikes stopping in the subsurface are generally coher-
 590 ent with the fact that most diking episodes do not lead to eruptions (e.g. Gudmunds-
 591 son, 1983, 1995), although more mechanisms that may stop dikes have been proposed
 592 than those that we model here, such as mechanical layering of host rock (Gudmundsson
 593 & Brenner, 2004; Geshi et al., 2012) and dike-fault interaction (Maccaferri et al., 2016).
 594 In further tests not reported here, SAM dikes with lower magma density (i.e. higher buoy-
 595 ancy) overcame such stress barriers, in accordance with previous models by Dahm (2000a);
 596 Maccaferri et al. (2011).

597 The outcomes of our synthetic scenarios, from the simplest to the more complex,
 598 show that dikes are deflected away from topographic lows (calderas), and attracted by
 599 topographic highs (hills, resurgent domes), even short-wavelength ones (e.g. a 5 km wide
 600 resurgent dome in STC-8). This is consistent with previous dike propagation and stress
 601 models considering topographic loading/unloading (Dahm, 2000a; Roman & Jaupart,
 602 2014; Corbi et al., 2016; Rivalta et al., 2019) and with results from gelatin-based ana-
 603 log models (Gaete et al., 2019; Mantiloni et al., 2021). Comparison to natural settings
 604 requires further discussion. The few synthetic scenarios we present here are not designed
 605 to reproduce the wide variety of vent patterns observed at real calderas. They do, nonethe-
 606 less, reproduce some common features of vent distribution in calderas. Scenarios STC-
 607 2 and STC-4,5,6,7 involve calderas lying on a coastline, with most or all dikes ending up
 608 on the mainland. This is compatible with vent patterns in similar worldwide settings,
 609 such as Campi Flegrei (Smith et al., 2011). In our tests, no dike trajectories end up within
 610 the caldera, except in STC-6 and STC-8. Among worldwide calderas, we find several ex-
 611 amples where past eruptive vents lie predominantly at or outside the caldera rim, as our
 612 model suggests: for instance, Alcedo, Cerro Azul, Darwin, Fernandina, Sierra Negra and
 613 Wolf calderas, Galápagos (Chadwick & Howard, 1991), or Aira caldera, Japan, (Geshi
 614 et al., 2020). Still, vents opening within a caldera can be observed in several other set-
 615 tings, like Newberry caldera, Oregon (MacLeod et al., 1982), Santorini caldera, Greece
 616 (Sigurdsson et al., 2006), or Campi Flegrei caldera, Italy (Smith et al., 2011). Intracaldera
 617 vent openings are predicted when the unloading pressure of the caldera is low or reduced
 618 by refilling (STC-6), or if large extensional tectonic stresses or resurgent domes are present
 619 (STC-8). Nonetheless, these three factors are not always associated with intracaldera
 620 vents in nature (e.g. no eruptions have occurred at Long Valley caldera’s resurgent dome
 621 after doming inception, Hildreth, 2004). Applying a model to a real caldera entails a deeper
 622 understanding of its evolution, stratigraphy and eruptive history, and requires dedicated
 623 work. For this reason, we chose not to apply our models to real calderas in this work,
 624 as running our model for a real scenario without a proper calibration of the stress state
 625 is no different than setting up a synthetic scenario with arbitrary stress. We remark, how-
 626 ever, that the fast dike propagation model we presented here is particularly suited for
 627 stress calibration procedures, such as the one by (Rivalta et al., 2019). This will be the
 628 subject of a future work.

629 Our model does not consider the viscous flow of magma within dikes and, as such,
 630 does not model dike velocity. The pathways predicted by our model, however, may be
 631 combined with existing models of dike velocity to integrate the two approaches (e.g. Pinel
 632 et al., 2017; Pansino et al., 2022).

633 In conclusion, we have developed a fast and flexible dike propagation model, that
 634 may complement the numerical model by Davis et al. (2020, 2021) over different appli-

635 cations. The outcomes of our synthetic scenarios are also consistent with observations
 636 at many real calderas. Stress models, however, are still critical and not yet fully under-
 637 stood. In a real-case application, our scenarios would be the end point of a stress cal-
 638 ibration, whereby the stress state of a volcanic region is constrained through a statisti-
 639 cal procedure aiming at matching dike simulations with observations, such as past vent
 640 locations (Rivalta et al., 2019), orientation of exposed dikes (Maerten et al., 2022) or fo-
 641 cal mechanisms (Zhan et al., 2022). Our model is well-suited for such purpose. Once the
 642 stress is calibrated, it may be used to perform a long-term forecast on future vent loca-
 643 tions, while the more sophisticated model may be employed to produce short-term prop-
 644 agation scenarios for incipient dike intrusions.

645 Acknowledgments

646 We are grateful to Kyle Anderson, Torsten Dahm, Francesco Maccaferri, Mehdi Nikkhoo
 647 and Virginie Pinel for constructive discussion and suggestions. L.M. is funded by the DFG
 648 grant N. RI 2782/6-1—ZO 277/3-1 within the MagmaPropagator project.

649 Data availability statement: the open-source Boundary-Element tool *Cut&Displace* is
 650 found at <https://doi.org/10.5281/zenodo.3694164>. The open-source Julia code used for
 651 TIM is found at <https://doi.org/10.5281/zenodo.4726796> and <https://doi.org/10.5281/zenodo.4727208>.
 652 The code for SAM and the data of the synthetic scenarios are available at *an open-access
 653 link to a Zenodo archive will be provided*.

654 References

- 655 Anderson, E. M. (1937). IX.—the dynamics of the formation of cone-sheets, ring-
 656 dykes, and caldron-subsidences. *Proceedings of the Royal Society of Edinburgh*,
 657 *56*, 128–157.
- 658 Bagnardi, M., Amelung, F., & Poland, M. P. (2013). A new model for the growth of
 659 basaltic shields based on deformation of fernandina volcano, galápagos islands.
 660 *Earth and Planetary Science Letters*, *377*, 358–366.
- 661 Branca, S., Carbone, D., & Greco, F. (2003). Intrusive mechanism of the 2002 ne-
 662 rift eruption at mt. etna (italy) inferred through continuous microgravity data
 663 and volcanological evidences. *Geophysical Research Letters*, *30*(20).
- 664 Cayol, V., & Cornet, F. H. (1998). Three-dimensional modeling of the 1983–1984
 665 eruption at piton de la fournaise volcano, réunion island. *Journal of Geophys-
 666 ical Research: Solid Earth*, *103*(B8), 18025–18037.
- 667 Cesca, S., Letort, J., Razafindrakoto, H. N., Heimann, S., Rivalta, E., Isken, M. P.,
 668 ... others (2020). Drainage of a deep magma reservoir near mayotte inferred
 669 from seismicity and deformation. *Nature Geoscience*, *13*(1), 87–93.
- 670 Chadwick, W. W., & Dieterich, J. H. (1995). Mechanical modeling of circumfer-
 671 ential and radial dike intrusion on galapagos volcanoes. *Journal of Volcanology
 672 and Geothermal Research*, *66*(1-4), 37–52.
- 673 Chadwick, W. W., & Howard, K. A. (1991). The pattern of circumferential and
 674 radial eruptive fissures on the volcanoes of fernandina and isabela islands,
 675 galapagos. *Bulletin of Volcanology*, *53*(4), 259–275.
- 676 Corbi, F., Rivalta, E., Pinel, V., Maccaferri, F., & Acocella, V. (2016). Under-
 677 standing the link between circumferential dikes and eruptive fissures around calderas
 678 based on numerical and analog models. *Geophysical Research Letters*, *43*(12),
 679 6212–6219.
- 680 Corbi, F., Rivalta, E., Pinel, V., Maccaferri, F., Bagnardi, M., & Acocella, V.
 681 (2015). How caldera collapse shapes the shallow emplacement and transfer
 682 of magma in active volcanoes. *Earth and Planetary Science Letters*, *431*,
 683 287–293.
- 684 Crouch, S. L., Starfield, A. M., & Rizzo, F. (1983). Boundary element methods in
 685 solid mechanics.

- 686 Dahm, T. (2000a). Numerical simulations of the propagation path and the arrest
687 of fluid-filled fractures in the earth. *Geophysical Journal International*, *141*(3),
688 623–638. doi: 10.1046/j.1365-246x.2000.00102.x
- 689 Dahm, T. (2000b). On the shape and velocity of fluid-filled fractures in the earth.
690 *Geophysical Journal International*, *142*(1), 181–192.
- 691 Davis, T., Bagnardi, M., Lundgren, P., & Rivalta, E. (2021). Extreme curva-
692 ture of shallow magma pathways controlled by competing stresses: insights
693 from the 2018 sierra negra eruption. *Geophysical Research Letters*, *48*(13),
694 e2021GL093038.
- 695 Davis, T., Healy, D., Bubeck, A., & Walker, R. (2017). Stress concentrations around
696 voids in three dimensions: The roots of failure. *Journal of Structural Geology*,
697 *102*, 193–207. doi: 10.1016/j.jsg.2017.07.013
- 698 Davis, T., Healy, D., & Rivalta, E. (2019). Slip on wavy frictional faults: Is the 3rd
699 dimension a sticking point? *Journal of Structural Geology*, *119*, 33–49. doi: 10
700 .1016/j.jsg.2018.11.009
- 701 Davis, T., Rivalta, E., & Dahm, T. (2020). Critical fluid injection volumes for un-
702 controlled fracture ascent. *Geophysical Research Letters*, e2020GL087774. doi:
703 10.1029/2020GL087774
- 704 Dieterich, J. H. (1988). Growth and persistence of hawaiian volcanic rift zones.
705 *Journal of Geophysical Research: Solid Earth*, *93*(B5), 4258–4270.
- 706 Dumont, Q., Cayol, V., Froger, J.-L., & Peltier, A. (2022). 22 years of satellite im-
707 agery reveal a major destabilization structure at piton de la fournaise. *Nature*
708 *Communications*, *13*(1), 1–11.
- 709 Ebinger, C., Ayele, A., Keir, D., Rowland, J., Yirgu, G., Wright, T., . . . Hamling,
710 I. (2010). Length and timescales of rift faulting and magma intrusion: The
711 afar rifting cycle from 2005 to present. *Annual Review of Earth and Planetary*
712 *Sciences*, *38*(1), 439–466.
- 713 Einarsson, P., Brandsdottir, B., et al. (1980). Seismological evidence for lateral
714 magma intrusion during the july 1978 deflation of the krafla volcano in ne-
715 iceland. *Journal of Geophysics*, *47*(1), 160–165.
- 716 Ferrante, G., Rivalta, E., & Maccaferri, F. (2022). Numerical simulation of magma
717 pathways and vent distribution in rifts from the early stages to maturity.
- 718 Gaete, A., Kavanagh, J. L., Rivalta, E., Hazim, S. H., Walter, T. R., & Dennis,
719 D. J. (2019). The impact of unloading stresses on post-caldera magma
720 intrusions. *Earth and Planetary Science Letters*, *508*, 109–121. doi:
721 10.1016/j.epsl.2018.12.016
- 722 Geshi, N., Kusumoto, S., & Gudmundsson, A. (2012). Effects of mechanical layering
723 of host rocks on dike growth and arrest. *Journal of Volcanology and Geother-
724 mal Research*, *223*, 74–82.
- 725 Geshi, N., Yamada, I., Matsumoto, K., Nishihara, A., & Miyagi, I. (2020). Accumu-
726 lation of rhyolite magma and triggers for a caldera-forming eruption of the aira
727 caldera, japan. *Bulletin of Volcanology*, *82*(6), 1–18.
- 728 Gómez-Vasconcelos, M. G., Villamor, P., Cronin, S. J., Palmer, A., Procter, J., &
729 Stewart, R. B. (2020). Spatio-temporal associations between dike intrusions
730 and fault ruptures in the tongariro volcanic center, new zealand. *Journal of*
731 *Volcanology and Geothermal Research*, *404*, 107037.
- 732 Grosfils, E. B., McGovern, P. J., Gregg, P. M., Galgana, G. A., Hurwitz, D. M.,
733 Long, S. M., & Chestler, S. R. (2015). Elastic models of magma reservoir
734 mechanics: a key tool for investigating planetary volcanism. *Geological Society,*
735 *London, Special Publications*, *401*(1), 239–267.
- 736 Gudmundsson, A. (1983). Form and dimensions of dykes in eastern iceland.
737 *Tectonophysics*, *95*(3-4), 295–307.
- 738 Gudmundsson, A. (1995). Infrastructure and mechanics of volcanic systems in ice-
739 land. *Journal of Volcanology and Geothermal Research*, *64*(1-2), 1–22.
- 740 Gudmundsson, A. (2002). Emplacement and arrest of sheets and dykes in cen-

- 741 tral volcanoes. *Journal of Volcanology and Geothermal Research*, 116(3-4),
742 279–298.
- 743 Gudmundsson, A. (2006). How local stresses control magma-chamber ruptures, dyke
744 injections, and eruptions in composite volcanoes. *Earth-science reviews*, 79(1-
745 2), 1–31.
- 746 Gudmundsson, A., & Brenner, S. L. (2004). How mechanical layering affects lo-
747 cal stresses, unrests, and eruptions of volcanoes. *Geophysical Research Letters*,
748 31(16).
- 749 Heimisson, E. R., Hooper, A., & Sigmundsson, F. (2015). Forecasting the path
750 of a laterally propagating dike. *Journal of Geophysical Research: Solid Earth*,
751 120(12), 8774–8792.
- 752 Hildreth, W. (2004). Volcanological perspectives on long valley, mammoth moun-
753 tain, and mono craters: several contiguous but discrete systems. *Journal of*
754 *Volcanology and Geothermal Research*, 136(3-4), 169–198.
- 755 Hildreth, W., Fierstein, J., & Calvert, A. (2017). Early postcaldera rhyolite and
756 structural resurgence at long valley caldera, california. *Journal of Volcanology*
757 *and Geothermal Research*, 335, 1–34.
- 758 Hjartardóttir, Á. R., Einarsson, P., Gudmundsson, M. T., & Högnadóttir, T. (2016).
759 Fracture movements and graben subsidence during the 2014 bárabunga dike
760 intrusion in iceland. *Journal of Volcanology and Geothermal Research*, 310,
761 242–252.
- 762 Ito, G., & Martel, S. J. (2002). Focusing of magma in the upper mantle through
763 dike interaction. *Journal of Geophysical Research: Solid Earth*, 107(B10),
764 ECV-6.
- 765 Jaeger, J., Cook, N., & Zimmermann, R. (2007). Fundamentals of rock mechanics.
766 blackwell, oxford.
- 767 Kervyn, M., Ernst, G., van Wyk de Vries, B., Mathieu, L., & Jacobs, P. (2009).
768 Volcano load control on dyke propagation and vent distribution: Insights from
769 analogue modeling. *Journal of Geophysical Research: Solid Earth*, 114(B3).
- 770 Kühn, D., & Dahm, T. (2008). Numerical modelling of dyke interaction and its in-
771 fluence on oceanic crust formation. *Tectonophysics*, 447(1-4), 53–65.
- 772 Le Corvec, N., Menand, T., & Lindsay, J. (2013). Interaction of ascending magma
773 with pre-existing crustal fractures in monogenetic basaltic volcanism: an ex-
774 perimental approach. *Journal of Geophysical Research: Solid Earth*, 118(3),
775 968–984.
- 776 Maccaferri, F., Bonafede, M., & Rivalta, E. (2010). A numerical model of dyke prop-
777 agation in layered elastic media. *Geophysical Journal International*, 180(3),
778 1107–1123. doi: 10.1111/j.1365-246X.2009.04495.x
- 779 Maccaferri, F., Bonafede, M., & Rivalta, E. (2011). A quantitative study of the
780 mechanisms governing dike propagation, dike arrest and sill formation. *Jour-
781 nal of Volcanology and Geothermal Research*, 208(1-2), 39–50. doi: 10.1016/j.
782 jvolgeores.2011.09.001
- 783 Maccaferri, F., Richter, N., & Walter, T. R. (2017). The effect of giant lateral col-
784 lapses on magma pathways and the location of volcanism. *Nature communica-
785 tions*, 8(1), 1–11.
- 786 Maccaferri, F., Rivalta, E., Keir, D., & Acocella, V. (2014). Off-rift volcanism in rift
787 zones determined by crustal unloading. *Nature Geoscience*, 7(4), 297–300. doi:
788 10.1038/ngeo2110
- 789 Maccaferri, F., Rivalta, E., Passarelli, L., & Aoki, Y. (2016). On the mechanisms
790 governing dike arrest: Insight from the 2000 miyakejima dike injection. *Earth*
791 *and Planetary Science Letters*, 434, 64–74.
- 792 MacLeod, N. S., Sherrod, D. R., Chitwood, L. A., & Jensen, R. A. (1982). *Geologic*
793 *map of newberry volcano, deschutes, klamath, and lake counties, oregon*. Geo-
794 logical Survey.
- 795 Maerten, F., Maerten, L., Plateaux, R., & Cornard, P. (2022). *Joint inversion*

- 796 *of tectonic stress and magma pressures using dyke trajectories* (Tech. Rep.).
 797 Copernicus Meetings.
- 798 Mantiloni, L., Davis, T., Gaete Rojas, A. B., & Rivalta, E. (2021). Stress inversion
 799 in a gelatin box: testing eruptive vent location forecasts with analog models.
 800 *Geophysical Research Letters*, *48*(6).
- 801 Martel, S. J., & Muller, J. R. (2000). A two-dimensional boundary element method
 802 for calculating elastic gravitational stresses in slopes. *Pure and Applied Geo-*
 803 *physics*, *157*(6-8), 989–1007. doi: 10.1007/s000240050014
- 804 Martí, J., Becerril, L., & Rodríguez, A. (2022). How long-term hazard assessment
 805 may help to anticipate volcanic eruptions: The case of la palma eruption 2021
 806 (canary islands). *Journal of Volcanology and Geothermal Research*, 107669.
- 807 McGarr, A., & Gay, N. (1978). State of stress in the earth’s crust. *Annual Review of*
 808 *Earth and Planetary Sciences*, *6*(1), 405–436.
- 809 McGuire, W., & Pullen, A. (1989). Location and orientation of eruptive fissures
 810 and feederdykes at mount etna; influence of gravitational and regional tectonic
 811 stress regimes. *Journal of Volcanology and Geothermal Research*, *38*(3-4),
 812 325–344.
- 813 McKenzie, D. (1978). Some remarks on the development of sedimentary basins.
 814 *Earth and Planetary science letters*, *40*(1), 25–32.
- 815 McTigue, D. F., & Mei, C. C. (1981). Gravity-induced stresses near topography
 816 of small slope. *Journal of Geophysical Research: Solid Earth*, *86*(B10), 9268–
 817 9278.
- 818 McTigue, D. F., & Mei, C. C. (1987). Gravity-induced stresses near axisymmetric
 819 topography of small slope. *International Journal for Numerical and Analytical*
 820 *Methods in Geomechanics*, *11*(3), 257–268.
- 821 Müller, B., Zoback, M. L., Fuchs, K., Mastin, L., Gregersen, S., Pavoni, N., . . .
 822 Ljunggren, C. (1992). Regional patterns of tectonic stress in europe. *Journal*
 823 *of Geophysical Research: Solid Earth*, *97*(B8), 11783–11803.
- 824 Muller, J. R., Ito, G., & Martel, S. J. (2001). Effects of volcano loading on dike
 825 propagation in an elastic half-space. *Journal of Geophysical Research: Solid*
 826 *Earth*, *106*(B6), 11101–11113. doi: 10.1029/2000JB900461
- 827 Muller, O. H., & Pollard, D. D. (1977). The stress state near spanish peaks, col-
 828 orado determined from a dike pattern. *Pure and Applied Geophysics*, *115*(1-2),
 829 69–86.
- 830 Nakada, S., Nagai, M., Kaneko, T., Nozawa, A., & Suzuki-Kamata, K. (2005).
 831 Chronology and products of the 2000 eruption of miyakejima volcano, japan.
 832 *Bulletin of Volcanology*, *67*(3), 205–218.
- 833 Neri, M., Rivalta, E., Maccaferri, F., Acocella, V., & Cirrincione, R. (2018). Etnean
 834 and hyblean volcanism shifted away from the malta escarpment by crustal
 835 stresses. *Earth and Planetary Science Letters*, *486*, 15–22.
- 836 Nikkhoo, M., & Walter, T. R. (2015). Triangular dislocation: an analytical, artefact-
 837 free solution. *Geophysical Journal International*, *201*(2), 1119–1141.
- 838 Orsi, G., De Vita, S., & Di Vito, M. (1996). The restless, resurgent campi flegrei
 839 nested caldera (italy): constraints on its evolution and configuration. *Journal*
 840 *of Volcanology and Geothermal Research*, *74*(3-4), 179–214.
- 841 Pansino, S., Emadzadeh, A., & Taisne, B. (2022). Modeling dike propagation in
 842 both vertical length and horizontal breadth. *Journal of Geophysical Research:*
 843 *Solid Earth*, e2022JB024593.
- 844 Pansino, S., & Taisne, B. (2019). How magmatic storage regions attract and repel
 845 propagating dikes. *Journal of Geophysical Research: Solid Earth*, *124*(1), 274–
 846 290.
- 847 Patrick, M. R., Houghton, B. F., Anderson, K. R., Poland, M. P., Montgomery-
 848 Brown, E., Johanson, I., . . . Elias, T. (2020). The cascading origin of the 2018
 849 kilauea eruption and implications for future forecasting. *Nature Communica-*
 850 *tions*, *11*(1), 1–13.

- 851 Pinel, V., Carrara, A., Maccaferri, F., Rivalta, E., & Corbi, F. (2017). A two-step
852 model for dynamical dike propagation in two dimensions: Application to the
853 july 2001 etna eruption. *Journal of Geophysical Research: Solid Earth*, *122*(2),
854 1107–1125.
- 855 Pollard, D. D. (1987). Elementary fracture mechanics applied to the structural inter-
856 pretation of dykes. In *Mafic dyke swarms* (Vol. 34, pp. 5–24).
- 857 Pollard, D. D., Fletcher, R. C., et al. (2005). *Fundamentals of structural geology*.
858 Cambridge University Press.
- 859 Pollard, D. D., & Holzhausen, G. (1979). On the mechanical interaction between a
860 fluid-filled fracture and the earth's surface. *Tectonophysics*, *53*(1-2), 27–57.
- 861 Rivalta, E., Corbi, F., Passarelli, L., Acocella, V., Davis, T., & Di Vito, M. A.
862 (2019). Stress inversions to forecast magma pathways and eruptive vent lo-
863 cation. *Science advances*, *5*(7), eaau9784. doi: 10.1126/sciadv.aau9784
- 864 Rivalta, E., Taisne, B., Bungler, A., & Katz, R. (2015). A review of mechanical
865 models of dike propagation: Schools of thought, results and future directions.
866 *Tectonophysics*, *638*, 1–42.
- 867 Roman, A., & Jaupart, C. (2014). The impact of a volcanic edifice on intrusive and
868 eruptive activity. *Earth and Planetary Science Letters*, *408*, 1–8. doi: 10.1016/
869 j.epsl.2014.09.016
- 870 Rubin, A. M. (1995). Propagation of magma-filled cracks. *Annual Review of Earth
871 and Planetary Sciences*, *23*(1), 287–336.
- 872 Rubin, A. M., & Gillard, D. (1998). Dike-induced earthquakes: Theoretical consider-
873 ations. *Journal of Geophysical Research: Solid Earth*, *103*(B5), 10017–10030.
- 874 Savage, W., Swolfs, H., & Amadei, B. (1992). On the state of stress in the near-
875 surface of the earth's crust. *Pure and Applied Geophysics*, *138*(2), 207–228.
- 876 Savage, W., Swolfs, H., & Powers, P. (1985). Gravitational stresses in long sym-
877 metric ridges and valleys. In *International journal of rock mechanics and min-
878 ing sciences & geomechanics abstracts* (Vol. 22, pp. 291–302).
- 879 Secor Jr, D. T., & Pollard, D. D. (1975). On the stability of open hydraulic fractures
880 in the earth's crust. *Geophysical Research Letters*, *2*(11), 510–513.
- 881 Sigmundsson, F., Hooper, A., Hreinsdóttir, S., Vogfjörð, K. S., Ófeigsson, B. G.,
882 Heimisson, E. R., ... others (2015). Segmented lateral dyke growth in a rifting
883 event at bárabunga volcanic system, iceland. *Nature*, *517*(7533), 191–195.
- 884 Sigurdsson, H., Carey, S., Alexandri, M., Vougioukalakis, G., Croff, K., Roman, C.,
885 ... others (2006). Marine investigations of greece's santorini volcanic field.
886 *Eos, Transactions American Geophysical Union*, *87*(34), 337–342.
- 887 Slim, M., Perron, J. T., Martel, S. J., & Singha, K. (2015). Topographic stress
888 and rock fracture: A two-dimensional numerical model for arbitrary topogra-
889 phy and preliminary comparison with borehole observations. *Earth Surface
890 Processes and Landforms*, *40*(4), 512–529.
- 891 Smith, V., Isaia, R., & Pearce, N. (2011). Tephrostratigraphy and glass composi-
892 tions of post-15 kyr campi flegrei eruptions: implications for eruption history
893 and chronostratigraphic markers. *Quaternary Science Reviews*, *30*(25-26),
894 3638–3660.
- 895 Smittarello, D., Smets, B., Barrière, J., Michellier, C., Oth, A., Shreve, T., ... oth-
896 ers (2022). Precursor-free eruption triggered by edifice rupture at nyiragongo
897 volcano. *Nature*, *609*(7925), 83–88.
- 898 Stephansson, O. (1988). Ridge push and glacial rebound as rock stress generators
899 in fennoscandia. *Bulletin of the Geological Institutions of the University of Up-
900 psala*, *14*, 39–48.
- 901 Tada, H., Paris, P., & Irwin, G. (2000). *American society of mechanical engineers.,
902 asm international., the stress analysis of cracks handbook*. ASME Press: Pro-
903 fessional Engineering Pub.: ASM International, New York.
- 904 Taisne, B., Tait, S., & Jaupart, C. (2011). Conditions for the arrest of a vertical
905 propagating dyke. *Bulletin of Volcanology*, *73*(2), 191–204.

- 906 Takada, A. (1997). Cyclic flank-vent and central-vent eruption patterns. *Bulletin of*
 907 *volcanology*, *58*(7), 539–556.
- 908 Townsend, M. R., Pollard, D. D., & Smith, R. P. (2017). Mechanical models for
 909 dikes: A third school of thought. *Tectonophysics*, *703*, 98–118.
- 910 Uhira, K., Baba, T., Mori, H., Katayama, H., & Hamada, N. (2005). Earthquake
 911 swarms preceding the 2000 eruption of miyakejima volcano, japan. *Bulletin of*
 912 *Volcanology*, *67*(3), 219–230.
- 913 Urbani, S., Acocella, V., Rivalta, E., & Corbi, F. (2017). Propagation and arrest
 914 of dikes under topography: Models applied to the 2014 bardarbunga (iceland)
 915 rifting event. *Geophysical Research Letters*, *44*(13), 6692–6701.
- 916 Ventura, G., Vilardo, G., & Bruno, P. P. (1999). The role of flank failure in mod-
 917 ifying the shallow plumbing system of volcanoes: an example from somma-
 918 vesuvius, italy. *Geophysical Research Letters*, *26*(24), 3681–3684.
- 919 Walter, T. R., Troll, V. R., Cailleau, B., Belousov, A., Schmincke, H.-U., Amelung,
 920 F., et al. (2005). Rift zone reorganization through flank instability in ocean
 921 island volcanoes: an example from tenerife, canary islands. *Bulletin of Vol-*
 922 *canology*, *67*(4), 281–291.
- 923 Weertman, J. (1971). Theory of water-filled crevasses in glaciers applied to verti-
 924 cal magma transport beneath oceanic ridges. *Journal of Geophysical Research*,
 925 *76*(5), 1171–1183.
- 926 Wright, T. J., Sigmundsson, F., Pagli, C., Belachew, M., Hamling, I. J.,
 927 Brandsdóttir, B., ... others (2012). Geophysical constraints on the dynamics
 928 of spreading centres from rifting episodes on land. *Nature Geoscience*, *5*(4),
 929 242–250.
- 930 Xu, W., & Jónsson, S. (2014). The 2007–8 volcanic eruption on jebel at tair island
 931 (red sea) observed by satellite radar and optical images. *Bulletin of Volcanol-*
 932 *ogy*, *76*(2), 1–14.
- 933 Xu, W., Jónsson, S., Corbi, F., & Rivalta, E. (2016). Graben formation and dike
 934 arrest during the 2009 harrat lunayyir dike intrusion in saudi arabia: Insights
 935 from insar, stress calculations and analog experiments. *Journal of Geophysical*
 936 *Research: Solid Earth*, *121*(4), 2837–2851.
- 937 Zhan, Y., Roman, D. C., Le Mével, H., & Power, J. A. (2022). Earthquakes indi-
 938 cated stress field change during the 2006 unrest of augustine volcano, alaska.
 939 *Geophysical Research Letters*, e2022GL097958.
- 940 Ziv, A., Rubin, A. M., & Agnon, A. (2000). Stability of dike intrusion along preex-
 941 isting fractures. *Journal of Geophysical Research: Solid Earth*, *105*(B3), 5947–
 942 5961.